Band offset engineering for p-SnO/n-mc-Si heterojunction solar cell

View Online · Export Citation · CrossMark

Lipika Mandal,[1] (iD) Syed Sadique Anwer Askari,[1,2] (iD) Manoj Kumar,[1] and Mukul Kumar Das[1,2,a] (iD)

AFFILIATIONS

[1]Department of Electronics Engineering, Indian Institute of Technology (Indian School of Mines), Dhanbad, Jharkhand 826004, India

[2]Centre of Excellence in Renewable Energy, Indian Institute of Technology (Indian School of Mines), Dhanbad, Jharkhand 826004, India

[a]Author to whom correspondence should be addressed: mukulkdas@iitism.ac.in

ABSTRACT

A cost-effective p-SnO_x/n-multicrystalline Si heterojunction thin film solar cell with SnO_x as an absorber layer is investigated by Technology Computer-Aided Design simulation using experimental values of the absorption coefficient of the SnO_x-layer. Heterointerface recombination and trapping of carriers due to the band offsets are considered in the simulation. Conduction and valence band offsets, which can be engineered by varying the growth kinetics dependent bandgap and electron affinity of SnO_x, play a significant role in enhancing the efficiency of the solar cell. A maximum conversion efficiency of 10.506% is obtained by a proper choice of affinity and bandgap for a particular thickness of the SnO_x-layer.

Tin oxide (SnO) as a transparent conductive oxide (TCO) layer, particularly for solar photovoltaic (PV) cells, has already been reported in the literature.[1–6] A few works on p-type SnO-based solar cell structures with a suitable n-type absorber[7,8] and a diode structure[2] have also been reported so far. In the reported solar cell structure, SnO is not used as an absorber layer. Direct optical transition and significant light absorption in p-type tin oxide (SnO_x) with controlled oxygen have been experimentally observed recently by the authors except the first one.[9] Therefore, the same oxide material with different oxygen mole fractions may be used as a p-type absorber as well as the TCO layer for solar cells. Now, the oxygen mole fraction can be controlled by controlling the partial oxygen pressure inside the chamber during growth of the thin SnO_x layer,[9] and fabrication of the device is expected to be of low cost mainly due to process simplicity. Also, the oxide material under consideration is non-toxic and inorganic in nature. So the solar cell structure, based on the oxide material, may be a prospective alternative of organic thin film solar cells, which suffers from the stability issue. However, the choice of suitable n-type material for making the p–n junction with p-SnO_x is important. In this work, multicrystalline silicon (mc-Si) is considered as material for the n-layer because it possesses nearly the same material parameters as crystalline silicon (c-Si), but at a much lower cost for fabrication of Si-wafers,[10] and Si is an obvious choice of material for its availability, matured fabrication

technology, and many other advantages. Moreover, it is expected that the deposition of the SnO_x thin film on the mc-Si wafer with a precisely controlled oxygen mole fraction, as on the Glass substrate,[9] is possible at room temperature. Thus, the proposed solar cell structure based on the junction between p-SnO_x and n-mc-Si would be cost effective.

Indeed, the performance of the thin film p-SnO_x/n-mc-Si solar cell will depend on the effect of the heterointerface between two different bandgap materials. As the oxide material properties like the bandgap, electron affinity, etc., can be tuned by controlling the oxygen pressure and other growth kinetics,[5,11,12] enhanced performance of the device can be obtained by suitable design of the device. In this work, performance analysis and design, mainly in terms of bandgap and affinity of the oxide material, for the p-SnO_x/n-mc-Si heterojunction solar cell using a SILVACO Technology Computer-Aided Design (TCAD) simulator are carried out. The effect of bulk and interface recombination along with the trapping of carriers by the barrier due to band-offsets is considered in the simulation.

The schematic structure of the device is shown in Fig. 1. A thin p-type tin oxide (p-SnO_x) layer on a 30 μm thick n-mc-Si-layer forms the heterojunction. A highly conductive SnO_y layer ($y > x$) forms the TCO layer. Highly doped (10^{19}/cm^3) n-type amorphous silicon (a-Si:H) with a thickness of 250 nm is taken as a back-surface field layer. Light is assumed to be incident on the wider bandgap, SnO layer,
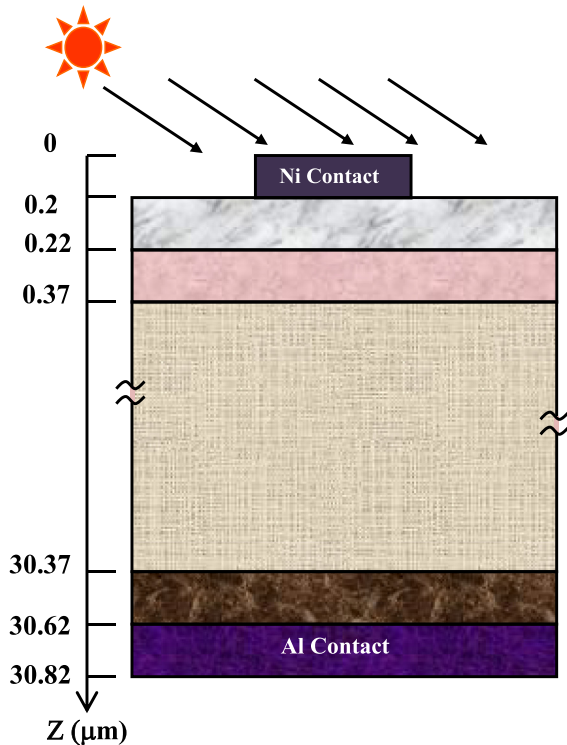
FIG. 1. Schematic structure of the proposed solar cell based on the SnO$_x$/Si hetero-junction solar cell.

FIG. 2. Energy band diagram at equilibrium for two different combinations of affinities and bandgaps of SnO$_x$: (a) both ΔE_C and ΔE_V positive, type-II heterostructure and (b) ΔE_C positive, ΔE_V negative, type-I heterostructure.

as shown in the figure. Front and rear contacts are considered to be made of nickel and aluminum to minimize the contact losses, respectively.

On incident of light, excess minority electrons in p-SnO$_x$ and minority holes in n-mc-Si are generated. These carriers, on account of their separation, may be lost due to recombination in the heterointerface trap states, which are created due to the lattice mismatch between two layers of different materials. Donor-like and acceptor-like trap levels, in the middle of the forbidden gaps of SnO$_x$ and mc-Si, respectively, are considered, as shown in Fig. 2, where the energy band diagram of the device besides the p–n junction is exposed. The concentration-dependent Shockley–Read–Hall (SRH) recombination model[13–15] is considered encompass the effect of the recombination on the performance of the device. Moreover, photo-generated carriers may be trapped by the barriers due to band offsets during their propagation. Conduction and valence band offsets, ΔE_C and ΔE_V, are defined as $\Delta E_C = \chi_{SnO} - \chi_{mc\text{-}Si}$ and $\Delta E_V = \chi_{SnO} - \chi_{mc\text{-}Si} + E_{g,SnO} - E_{g,mc\text{-}Si}$, respectively, where χ_{SnO} and $\chi_{mc\text{-}Si}$ are affinities of SnO$_x$ and mc-Si, respectively, and $E_{g,SnO}$ and $E_{g,mc\text{-}Si}$ are the bandgaps of SnO$_x$ and mc-Si, respectively. Depending on the polarity of these band offsets, type-II or type-I heterostructures are formed as shown in Figs. 2(a) and 2(b), respectively. Now, the carriers are considered to be trapped when the band-offsets are positive. Now, some of these trapped carriers are considered to be emitted through a slow thermionic emission process and some are lost due to recombination, depending on the carrier lifetime and emission rate. Since the barrier width is on the order of a few tens on nanometers here, tunneling of
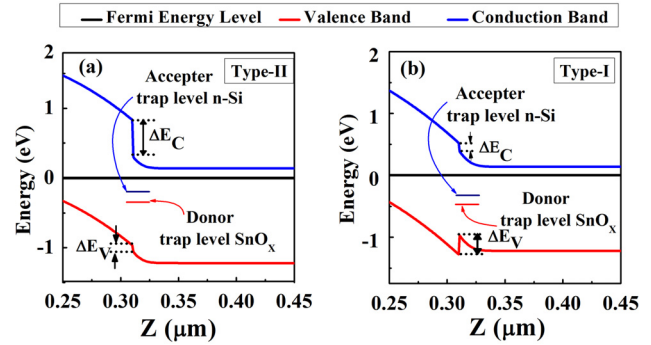
the carrier is neglected. As the electric fields at the heterointerfaces are high, field-dependent mobility has also been considered in this study.

TCAD simulation of the device is performed by varying the bandgap and affinity with an upper boundary of ionization potential of SnO$_x$, which is 5.8 eV (Ref. 1), owing to the feasibility of p-type conductivity of SnO$_x$. Some important material parameters, used in simulation, along with their sources are tabulated in Table I for quick reference. Wavelength-dependent refractive indices of different materials are taken from the literature.[9,16] Short circuit current density (J_{SC}), open circuit voltage (V_{OC}), fill factor (FF), and power conversion efficiency (PCE) of the proposed solar cell are extracted from simulated I–V curves. J_{SC} as a function of χ_{SnO} for different $E_{g,SnO}$ values is shown in Fig. 3(a). In this figure, the thickness of the SnO$_x$ layer and the interface defect density are kept fixed at 50 nm and 10^{13}/cm^2, respectively. An initial increment, then a sharp decrement after reaching a peak, and an almost constant value of J_{SC} with the increase in affinity for a fixed bandgap of SnO are observed. This is due to the combined effect of the electric field and band offset variations with SnO$_x$ affinity as shown in Fig. 3(b) and in the inset of Fig. 3(a) (INSET-a), respectively. For understanding the J_{SC} variation, let us consider the case of a particular bandgap, say 1.8 eV. Positional variation of the electric field for some vital affinity points, where the rate of change of J_{SC} in Fig. 3(a) is significant, at the said bandgap is shown in Fig. 3(b). The fields in the fully depleted SnO$_x$ region and in the depleted portion of the Si layer are shown in the figure. With the

TABLE I. Some important material parameters used in the simulation.

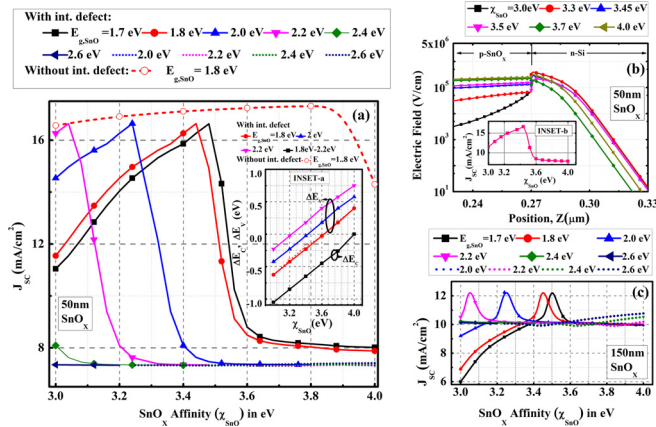| Parameter	p-SnO$_x$	n-mc-Si	n-Si[10]
E_g (eV)	1.8–2.8[3,6,9,18]	1.4[10]	1.7
χ (eV)	3.5–5[1,3,19]	4.05[10]	4.05
μ_n (cm^2/V S)	3[20]	500[17]	1000
μ_p (cm^2/V S)	3[20]	100[17]	500
N_D (cm^{-3})	1.0×10^{17}	...	...
N_A (cm^{-3})	...	1.0×10^{18}	1.0×10^{19}
τ_n (S)	4×10^{-9} (Ref. 21)	4.0×10^{-7} (Ref. 17)	50×10^{-6}
τ_p (S)	4×10^{-9} (Ref. 21)	4.0×10^{-7} (Ref. 17)	50×10^{-6}

FIG. 3. (a) and (c) Plot of J_{SC} vs SnO_x affinity for its different bandgaps, considering the interface defect density, 10^{13}/cm², for different thicknesses of SnO_x, (a) 50 nm along with the case of zero defect density for the 1.8 eV bandgap and with INSET-a and band offsets vs SnO_x affinity for different bandgaps, (c) 150 nm; (b) positional variation of the electric field for some affinities of SnO_x with INSET-b and J_{SC} vs SnO_x affinity for its bandgap of 1.8 eV.

increasing affinity, the electric field at the interface increases. Additionally, the field in the whole SnO layer increases, and for the depleted region of the Si layer, it initially remains constant (3.0 eV, 3.3 eV), then decreases (3.45 eV, 3.5 eV, 3.7 eV), and, after that, increases (4.0 eV). As the electric field-dependent mobility, within the saturation velocity limit, and SRH recombination due to the bulk and interface defects are considered, the total number of carriers, which contribute to the photocurrent after recombination loss, will depend on the value of the electric field integrated over Z in the range covering depleted portion of both the p and n layers. Positional variation of electric fields for different values of SnO_x affinities in Fig. 3(b) implies that J_{SC} increases initially with the affinity, and after reaching a peak (nearly at 3.45 eV affinity for the 1.8 eV bandgap), it decreases as shown in Fig. 3(a) and also in INSET-b. However, beyond 3.6 eV affinity, instead of increasing, as expected from the enhanced value of the integrated electric field, J_{SC} decreases slightly. Because of the effect of carrier trapping at the barrier due to band offsets, minority hole trapping due to positive ΔE_V with a significant absolute value (INSET-a) here becomes significant for this range of affinity. Current density variations for other bandgaps also follow the electric field variation and the effect of carrier trapping. However, the peaks in J_{SC} shift toward lower affinities for higher bandgaps. This is due to the attaining of the maximum integrated electric field at lower affinities. It may be mentioned here that the peaks for 2.4 eV and 2.6 eV bandgaps are not visible for the considered range of affinity. As the upper limit of ionization potential (sum of affinity and bandgap) of SnO_x is considered to be 5.8 eV, some portions of the graphs beyond the above potential limit are shown by dotted lines. The effect of interface recombination can be understood by comparing the results with a plot for zero interface defect density, which is shown in the same figure by the dashed line. Here, J_{SC} initially increases with a higher slope, unlike the case of nonzero defect density, and decreases after a particular affinity. This can also be explained from electric field variation, which is not shown here as the field variation is the same but with a difference in its values

compared to the case of nonzero defect density. As the recombination due to bulk defects affects the photocurrent, it is expected to be dependent on the SnO_z layer thickness also. This can be observed from Fig. 3(c) where J_{SC} variation is shown for a larger thickness of 150 nm but for the same defect density. The nature of variation is similar to that for the lower thickness except that the smaller values of J_{SC} are obtained here. This is mainly due to the enhanced bulk recombination of photogenerated carriers for the larger SnO_x-layer thickness.

Open circuit voltage (V_{OC}) is determined by the separation of quasi-Fermi levels, and for a heterostructured cell, it depends on ΔE_C and ΔE_V in addition to its normal dependency on material parameters. For type-I and type-II heterostructured solar cells, V_{OC} is governed, respectively, by the following relationships:

$$V_{oc} = (E_{g,SnO} + E_{g,Si})/2q + (|\Delta E_v| - |\Delta E_c|)/2q + kT/q[\ln(N_a N_d / N_{cn} N_{vp})],$$

$$V_{oc} = (E_{g,SnO} + E_{g,Si})/2q + (|\Delta E_v| + |\Delta E_c|)/2q + kT/q[\ln(N_a N_d / N_{cn} N_{vp})],$$

where k is the Boltzmann constant, T is the absolute temperature, $N_a(N_d)$ is the acceptor (donor) concentration, and $N_{cn}(N_{vp})$ is the density of states for conduction band (CB) in the n-layer [valence band (VB) in the p-layer]. Variations of V_{OC} with SnO affinities are shown in Figs. 4(a) and 4(b) for two different thicknesses, 50 nm and 150 nm, respectively. It is seen that V_{OC} initially increases and becomes almost constant for all the bandgaps. The variation can be understood from band offset variation, as shown in the INSET-a, along with the above expressions of V_{OC} for type-I and type-II heterostructures.
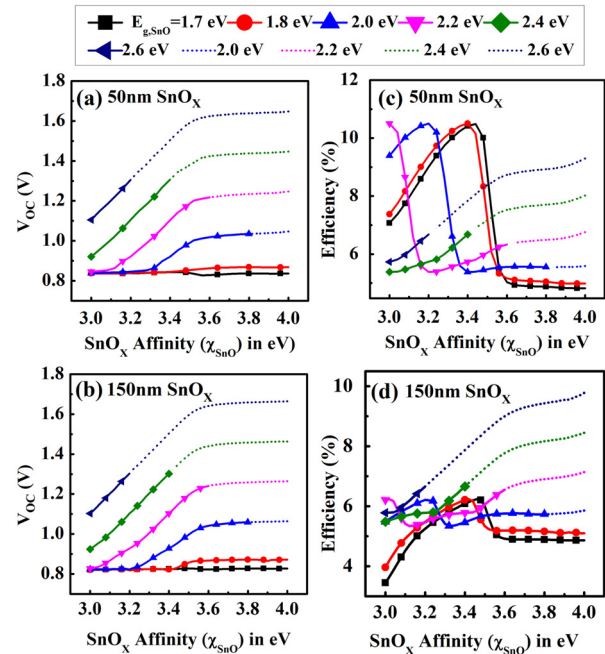

FIG. 4. Variation of V_{OC} (a) and (b) and efficiency (c) and (d) with SnO_x affinity for its different bandgaps with the interface defect density, 10^{13}/cm², for the thickness of SnO_x (a) and (c) 50 nm and (b) and (d) 150 nm.

TABLE II. Some best possible values of SnO$_x$ parameters for maximum efficiency of the solar cell.

Thickness (nm)	Band gap (eV)	Electron affinity (eV)	Maximum efficiency (%)
50	2.0	3.2	10.506
50	2.2	3.0	10.506
90	1.8	3.4	8.524
90	2.0	3.2	8.524
150	2.4	3.4	6.66
150	2.6	3.2	6.66

Overall performance of the solar cell can be gauged by analyzing its power conversion efficiency (PCE), which depends on V_{OC}, J_{SC}, and, another important parameter, fill factor (FF). It has been observed that the FF also varies with bulk and interface effects as a consequence of J_{sc} and V_{oc} variations, which has been shown earlier. Efficiency variations for 50 nm and 150 nm thicknesses of the SnO$_x$ layer, are shown in Figs. 4(c) and 4(d), respectively. This study has been extended for an in-between thickness, namely, 90 nm, and some best possible designs (affinity and bandgap combinations for different SnO$_x$ thicknesses) of the device for its maximum efficiency are summarized in Table II for ready reference.

Performance analysis of the p-SnO$_x$/n-mc-Si heterojunction thin film solar cell has been carried out by TCAD simulation, considering the bulk and heterointerface recombination as well as the effect of band offsets. Experimental values of the absorption coefficient of SnO$_x$, reported elsewhere by the authors except the first author, are considered in the simulation. Some best possible designs of the device in terms of its efficiency are obtained. Band offsets between SnO$_x$ and mc-Si, which can be controlled by varying χ_{SnO}, $E_{g,SnO}$, and thickness of the SnO$_x$ layer, are taken into account in obtaining the design. A maximum conversion efficiency of 10.506% is obtained for the 90 nm thick SnO$_x$ layer for a particular combination of its affinity and bandgap.

See the supplementary material for fill factor (FF) variation.

DATA AVAILABILITY

The data that support the findings of this study are available within this article and its supplementary material.

REFERENCES

[1]K. J. Saji, Y. P. V. Subbaiah, K. Tian, and A. Tiwari, Thin Solid Films **605**, 193–201 (2016).

[2]K. Javaid, Y. F. Xie, H. Luo, M. Wang, H. L. Zhang, J. H. Gao, and F. Zhuge, Appl. Phys. Lett. **109**, 123507 (2016).

[3]W. Guo, L. Fu, Y. Zhang, K. Zhang, L. Y. Liang, Z. M. Liu, H. T. Cao, and X. Q. Pan, Appl. Phys. Lett. **96**, 042113 (2010).

[4]T. Yang, J. Zhao, X. Li, X. Gao, C. Xue, Y. Wu, and R. Tai, Mater. Lett. **139**, 39–41 (2015).

[5]L. Y. Liang, Z. M. Liu, H. T. Cao, and X. Q. Pan, Appl. Mater. Interfaces **2**(4), 1060–1065 (2010).

[6]J. B. Varley, A. Schleife, A. Janotti, and C. G. Van De Walle, Appl. Phys. Lett. **103**, 082118 (2013).

[7]K. Javaid, W. Wu, J. Wang, J. Fang, H. Zhang, J. Gao, F. Zhuge, L. Liang, and H. Cao, ACS Photonics **5**(6), 2094–2099 (2018).

[8]K. Javaid, J. Yu, W. Wu, J. Wang, H. Zhang, J. Gao, F. Zhuge, L. Liang, and H. Cao, Phys. Status Solidi RRL **12**, 1700332 (2018).

[9]M. Kumar, S. S. A. Askari, and M. K. Das, Mater. Lett. **257**, 126684 (2019).

[10]See http://silvaco.com for "Silvaco 2016 Atlas User's Manual 2016 Version."

[11]J. A. C. Frescas, P. K. Nayak, H. A. Al-Jawhari, D. B. Granato, U. Schwingenschlögl, and H. N. Alshareef, ACS Nano **7**, 5160–5167 (2013).

[12]L. Guo, M. Zhao, D. Zhuang, Q. Gong, H. Tan, M. Cao, and L. Ouyang, Mater. Sci. Semicond. Process. **46**, 35–38 (2016).

[13]S. S. A. Askari, M. Kumar, and M. K. Das, Semicond. Sci. Technol. **33**, 115003 (2018).

[14]R. N. Hall, Phys. Rev. **87**, 387 (1952).

[15]W. Shockley and W. T. Read, Phys. Rev. **87**, 835–842 (1952).

[16]T. Toyama, Y. Seo, T. Konishi, H. Okamoto, R. Morimoto, Y. Nishikawa, and Y. Tsutsumi, Thin Solid Film **555**, 148–152 (2014).

[17]H. Keshtkar, H. Mansourghanaei, E. Javadiun, and P. Rahimi, in Proceedings of the IEEE International Conference on Electro Information Technology (EIT), Lincoln, NE (2017), pp. 177–181.

[18]Q. J. Liu, H. T. Liu, and L. P. Feng, Comput. Mater. Sci. **47**, 1016–1022 (2010).

[19]X. Li, L. Liang, H. Cao, R. Qin, H. Zhang, J. Gao, and F. Zhuge, Appl. Phys. Lett. **106**, 132102 (2015).

[20]Y. Ogo, H. Hiramatsu, K. Nomura, H. Yanagi, T. Kamiya, M. Kimura, and M. Hirano, Phys. Status Solidi A **206**(9), 2187–2191 (2009).

[21]Z. G. Li, H. Cao, A. Song, L. Liang, X. Wu, J. Yang, and Y.-L. Song, Appl. Phys. Lett. **110**, 172102 (2017).